

A Characterization of the Circumstellar Gas around WD 1124-293 using Cloudy

AMY STEELE,¹ JOHN DEBES,² SIYI XU (许偲艺),³ SHERRY YEH,⁴ AND PATRICK DUFOUR⁵

¹*University of Maryland at College Park*

²*Space Telescope Science Institute*

³*NSF's NOIRLab/Gemini Observatory, 670 N. A'ohoku Place, Hilo, Hawaii, 96720, USA*

⁴*W. M. Keck Observatory*

⁵*Université de Montreal*

ABSTRACT

Between 30 - 50% of white dwarfs (WDs) show heavy elements in their atmospheres. This “pollution” is thought to arise from the accretion of planetesimals perturbed by outer planet(s) to within the WD’s tidal disruption radius. A small fraction of these WDs show either emission or absorption from circumstellar (C-S) gas. The abundances of metals in the photospheres of WDs with C-S gas are mostly similar to the bulk composition of the Earth. The C-S component arises from gas produced through collisions and/or the sublimation of disintegrating planetesimals. High resolution spectroscopic observations of WD 1124-293 reveal photospheric and C-S absorption of Ca in multiple transitions. Here, we present high signal-to-noise ratio spectra, an updated WD atmosphere analysis, and a self-consistent model of its C-S gas. We constrain the abundances of Ca, Mg, and Fe in the photosphere of WD 1124-293, and find agreement with the abundances of these 3 species in the C-S gas. We find the location of the C-S gas is about a hundred white dwarf radii, the C-S and photospheric compositions are thus far consistent, the gas is not isothermal, and the amount of C-S Ca has not changed in two decades. We also demonstrate how to use Cloudy to model C-S gas viewed in absorption around polluted WDs. Modeling the abundances of C-S gas around polluted WDs with Cloudy provides a new method to measure the composition of exo-planetesimals and will allow a direct comparison to the composition of rocky bodies in the Solar System.

Keywords: DA stars (348), DB stars (358), Circumstellar gas(238), Circumstellar matter(241)

1. INTRODUCTION

The spectra of white dwarfs (WDs) should show only pressure-broadened hydrogen and/or helium absorption lines, yet at least 27% of young WDs with temperatures less than $\sim 27,000$ K have photospheres polluted by elements heavier than helium (Koester et al. 2014). These metals should settle out of the atmospheres of WDs on timescales of days to Myr depending on the WD temperature, surface gravity, and main atmospheric composition (H vs. He) (Koester 2009). For isolated WDs, the pollution could arise from grains in the interstellar medium (ISM) (Dupuis et al. 1993a,b), or more likely, from the accretion of solids that have been liberated from a captured planetesimal (e.g. WD 1145+0171 Vanderburg et al. 2015). The gas phase of the latter accre-

tion process can exist as a circumstellar disk observable as a double peaked line in emission (e.g. Manser et al. 2016) or a Doppler broadened profile in absorption (e.g. Xu et al. 2016). WD 1124-293 is one of a few WDs that shows both metal photospheric absorption and circumstellar absorption features.

We investigate the gas toward WD 1124-293 to explore the conditions necessary to produce the observed absorption. WD 1124-293 is of spectral type DAZ (a hydrogen dominated atmosphere with metal lines), has an effective temperature $T_{\text{eff}} \sim 9367$ K, and surface gravity $\log g = 7.99$ (see Table 1). The one observed C-S Ca K absorption feature detected at 8σ (Debes et al. 2012) provides an opportunity to explore the physical conditions that result in this type of spectrum. We use the microphysics code, Cloudy, to model the metal-rich gas polluting WD 1124-293 by creating a grid of models of C-S gas to explore the abundances of elements from He to Zn relative to hydrogen. Due to the lack of an infrared

Table 1. Properties of WD 1124-293

Parameter	Value	Reference
RA, Dec (J2000)	11:27:09.25, −29:40:11.20	^a
Spectral Type	DAZ	^b
G (mag)	15.0139	^a
T_{wd} (K)	9367	^c
$\log g$ (cm s^{-2})	7.99	^c
R_{wd} (R_{\odot})	0.0127	^c
M_{wd} (M_{\odot})	0.575	^c
Luminosity (L_{\odot})	0.00111	^c
Distance (pc)	33.691	^a

NOTE—^aGaia Collaboration et al. (2018), ^bSubasavage et al. (2017), ^cfrom <http://www.montrealwhitedwarfdatabase.org/evolution.html>

excess (Barber et al. 2016), we exclude grains from our models. From the code, we obtain line optical depths, species column densities, and the temperature profile through the gas cloud. With these models, we place constraints on the potential masses and abundances of the C-S gas.

In Section 2, we present new observations of WD 1124-293 with Keck HIRES and an improved co-added MIKE spectrum. In Section 3, we describe how we know the pollution of WD 1124-293 visible in the new, higher resolution HIRES spectrum is not due to the ISM. In section 4, we describe how we model a polluted white dwarf with Cloudy and apply this method to WD 1124-293, showing how we can determine the characteristics of its C-S gas using Cloudy. In short, we build a grid of models and place constraints on the column densities needed for detecting features. In section 5, we present our results and conclude in section 6.

2. OBSERVATIONS

WD 1124-293 was observed 16 times between 1998 and 2011 (Debes et al. 2012) with the MIKE echelle spectrograph (Bernstein et al. 2003). We observed WD 1124-293 using the HIRES echelle spectrograph (Vogt et al. 1994) on the Keck I telescope for 1200s on April 24, 2018. For the HIRES observations, the blue collimator and C5 decker were used with a slit width of 1.148 arcsec, typically giving a spectral resolution of $\sim 40,000$. However, the seeing during the observation was ~ 0.5 arcsec, and the effective resolution is $\sim 80,000$. The data were reduced with the MAKEE package. The Ca K line was extracted over two orders and averaged, while the H line was extracted over one order. We continuum-normalized 10 Å regions of the spectrum by fitting a

Table 3. Keck/HIRES Observations of WD 1124-293 and Standards

Target	Dist (pc)	Sep (")	Exp (s)
WD 1124-293	33.7	—	1200s
HIP56280A	26.3	79	30s
HIP56280B	26.3	79	30s
HIP55864	117	16	100s
HIP55901	401	24.6	100s

NOTE—The distance, separation from WD 1124-293, and exposure time for the target and standards. The observation date was April 24, 2018, at a resolution $\sim 40,000$ with a wavelength range of 3100 - 5950 Å.

polynomial to the continuum to remove effects due to the instrument response function. The signal-to-noise (S/N) ratio is ~ 38 in a 10 Å region (3935 Å to 3945 Å), which corresponds to ~ 75 per resolution element. We detect C-S and photospheric absorption at the Ca K line and only photospheric absorption at the Ca H line. We report that no new absorption or emission features have been detected.

Additionally, we reanalyzed the many epochs of spectra presented in Debes et al. (2012). The multiple MIKE epoch spectroscopy was extracted over two orders that contained the Ca H and K lines. For this work, we took the reduced spectra of WD 1124-293 from both the red and blue CCDs at each epoch and flux calibrated the orders against a model DA atmosphere (Koester 2010)¹ with the appropriate T_{eff} and $\log g$ (see Table 1) based on WD 1124-293’s parallax and spectro-photometry from APASS, 2MASS, and ALLWISE catalogs. Once all epochs were flux calibrated, we median combined the spectra to a common wavelength grid with a sampling of 0.05 Å between 3350 Å and 5030 Å and 0.08 Å between 5030 Å and 9400 Å. The typical resolution for the MIKE spectra is $\sim 34,000$. Near the Ca K line, the final S/N ratio of the data as measured in the continuum corresponds to ~ 194 per resolution element.

We present the Ca absorption line properties for WD 1124-293 in Table 2 for the co-added MIKE spectrum and Keck HIRES spectrum presented in this work. We fit the circumstellar and photospheric absorption features with Gaussians to calculate the equivalent widths of the lines, as well as the FWHMs. The photospheric lines are gravitationally red-shifted. All line center ve-

¹ <http://svo2.cab.inta-csic.es/theory/newov2/index.php>

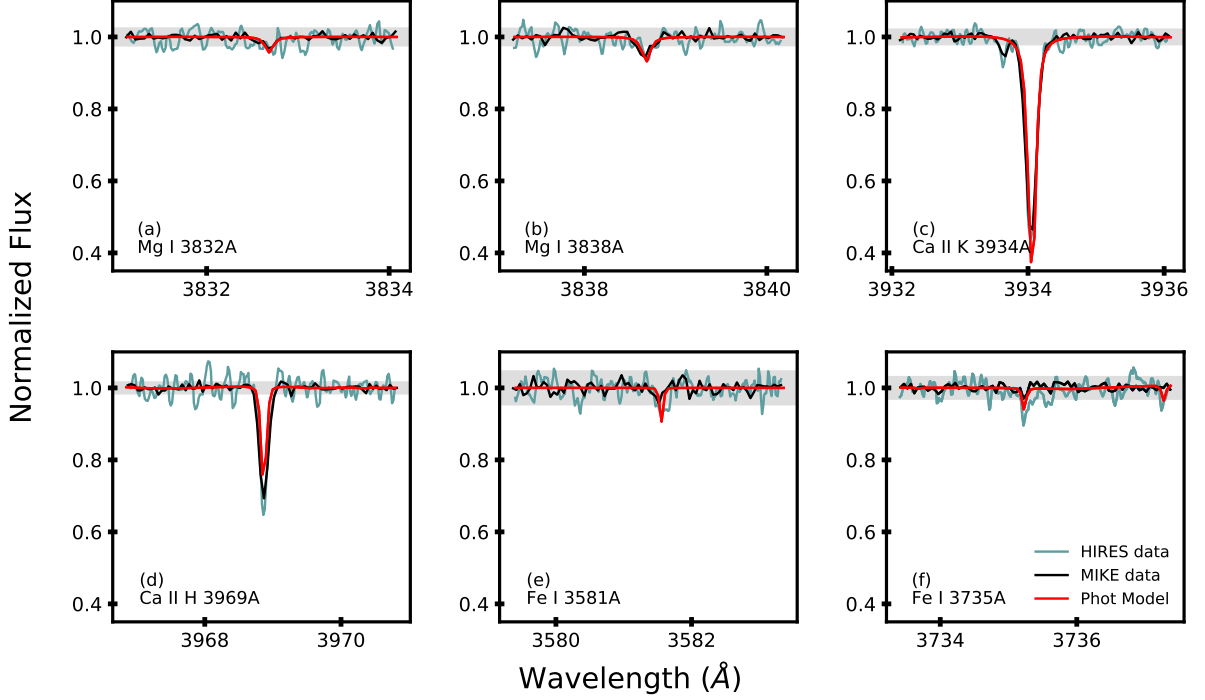


Figure 1. Detection of metal photospheric absorption lines for WD 1124-293 using a co-added MIKE spectrum. For each square panel, the MIKE data are shown in black, new Keck HIRES data are shown in teal, and a model of the photosphere is shown in red. The model is convolved with a Gaussian kernel with a width determined by a resolution, $R = 60,000$ using a routine from PyAstronomy (<https://github.com/sczesla/PyAstronomy>, Czesla et al. 2019). The gray region highlights a $\pm 3\sigma$ region for the MIKE spectra.

Table 2. Ca absorption line properties for WD 1124-293

Dataset	Ca K : $\lambda_0 = 3933.6614 \text{ \AA}$, Ca H : $\lambda_0 = 3968.4673 \text{ \AA}$									
	Circumstellar				Photospheric					
	λ_c	v_c	Eq Width	FWHM	λ_c	v_c	Eq Width	λ_c	v_c	Eq Width
	(\AA)	(km/s)	(m \AA)	(km/s)	(\AA)	(km/s)	(m \AA)	(\AA)	(km/s)	(m \AA)
MIKE	3933.623	-2.9	7.1	9.91	3934.020	27.3	113 ± 2	3968.841	28.25	52 ± 1
HIRES	3933.637	-1.9	7.8	5.97	3934.053	29.8	105 ± 1.5	3968.879	31.1	65 ± 3

NOTE—The Ca H and K line wavelengths are given in air. We only detect a C-S feature at the Ca K line. For the C-S line, the central wavelength of the line is λ_c , the Doppler shift velocity is v_c , the equivalent width of the line assuming a Gaussian profile is “Eq Width,” and the full width at half max is FWHM.

locities for the Ca K and H lines are also presented in Table 2. The HIRES dataset has the highest resolution of the three sets, and so we use it to constrain the location of the gas. The co-added MIKE spectrum has the highest S/N, so we use it to constrain the abundances of different species. In Figure 1, we show selected photospheric absorption features due to Mg, Ca, and Fe that appear in both the co-added MIKE spectrum and new HIRES spectrum.

3. POLLUTION AND THE ISM

Debes et al. (2012) first investigated the possibility that the weak Ca absorption detected towards WD 1124-293 could be explained by coincident local ISM absorption by comparing against high SNR spectra of stars located closely in the sky. For that study, Debes et al. (2012) looked at HIP 56280A, HIP 55864, HIP 55731, HIP 55901, and HIP 55968, but did not have sufficient parallax information on all of the stars to correctly sort them in terms of increasing distance from the Earth.

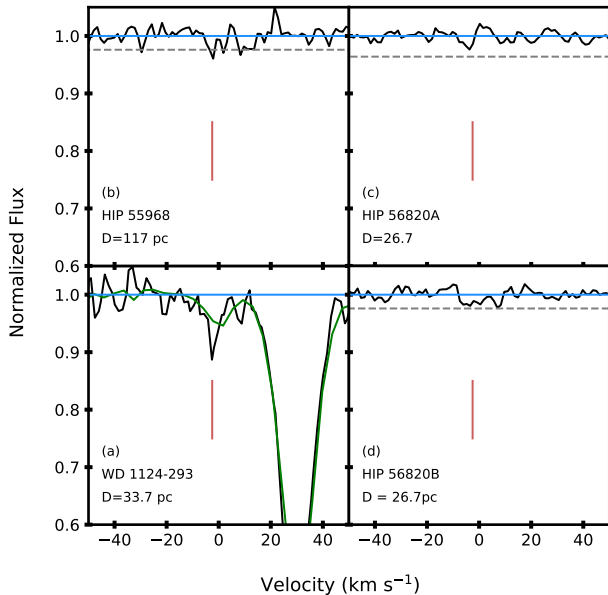


Figure 2. The normalized flux for the (a) target and nearby sources (b) - (d) HIP 56280A, HIP 56280B, and HIP 55864. For all panels, the blue line is drawn at a value of 1.0 to guide the eye, the 2019 HIRES data are shown in black, and the red vertical line gives the approximate velocity of the C-S line for WD 1124-293, -2.5 km s^{-1} . In panels (b) - (d), the dashed gray is drawn at 3σ below the continuum. In panel (a), the green curve is the normalized flux from the Magellan MIKE observations described in Debes et al. (2012).

With the advent of the Gaia mission, secure parallaxes now exist for that sample of stars. We re-observed HIP 56280A, HIP 55901, and HIP 55864 and in addition observed HIP 56280B, the physically bound companion to HIP 56280A. HIRES has higher spectral resolution compared to MIKE, and thus higher sensitivity to weak spectral features. The addition of HIP 56280B also ensures tighter constraints on the amount of Ca present in the ISM interior to $\sim 30 \text{ pc}$ with two independent measurements of that part of the sky.

In order to search for weak lines from the ISM we first had to fit and remove the continuum near the expected rest frame velocity of the Ca K line in question for each standard star. This was relatively straightforward for HIP 55901 and HIP 55864, which show broad Ca absorption due to the rapid rotation of the host stars—the continuum can be fit with a high order polynomial (Debes et al. 2012).

Our approach for HIP 56820A and HIP 56820B was slightly different, due to the later spectral type of these two stars. Both objects are roughly consistent with F stars and are likely nearly the same effective temperature and gravity. Both stars show Ca emission in the line core due to stellar activity, though HIP 56820A shows

stronger emission. For both stars we fit the broad Ca component with a spline fit and then fit the Ca line core with a two component Gaussian curve. We verified that our fits did not unintentionally fit any absorption lines coincident with the rest velocity of the C-S line seen in WD 1124-293. Our resulting continuum fit lines are shown in Figure 2, along with the expected 3σ upper limit to detectable absorption for each star. We estimated this upper limit by taking the standard deviation of flux in the normalized spectra, assuming that we would detect anything 3σ below the continuum level. We note that we do not show the spectrum of HIP 55901, which shows strong absorption consistent with that observed previously in Debes et al. (2012). None of these comparison stars near WD 1124-293 show Ca absorption at the velocity of the observed Ca line, so we confidently rule out an ISM contribution to the WD spectrum.

4. MODELING WD CIRCUMSTELLAR GAS WITH CLOUDY

4.1. Cloudy Model Inputs

We aim to constrain the abundances of metals in the circumstellar gas of WD 1124-293. A Cloudy input file requires an ionizing source, the geometry of the gas, the density of hydrogen in the gas, and the abundances of He to Zn, relative to H. In this section, we describe how we determine these inputs for WD 1124-293 and how we use the Cloudy output, thereby describing our method for using Cloudy to model the C-S environment of a polluted white dwarf. Calculations were performed with version 17.01 of Cloudy, last described by Ferland et al. (2017).

4.1.1. The ionizing source

For the Cloudy model, we use an interpolated Koester DA photosphere (Koester 2010; Tremblay, & Bergeron 2009)² with a temperature of 9420 K and luminosity of $0.00111L_{\odot}$ as the input, or ionizing continuum. The continuum is mapped to an energy mesh with a resolution of 0.05, (20x the native course grid of $R \sim 300$).

4.1.2. Geometry

The geometry of the C-S gas around WD 1124-293 is unknown. We choose to set the geometry in a disk, rather than a sphere because we have shown that it is highly unlikely that the ISM is the source of the pollution. Debes et al. (2012) place constraints on the location of the C-S gas, with a minimum distance of

² Models were downloaded from the Spanish Virtual Observatory database.

$7_{-3}^{+11} R_{\text{wd}}$, maximum distance of 32000 AU, and dynamical estimate of $\sim 54 R_{\text{wd}}$, where R_{wd} is the radius of WD 1124-293. The dynamical estimate of the location of the gas is determined assuming the gas is in a circular Keplerian orbit and using the FWHM of the gas absorption feature to determine the upper limit to the disk's orbital velocity. The “dynamical” distance of the gas from the WD, R_{Kep} , is

$$R_{\text{Kep}} \approx (GM_{\text{wd}})^{1/3} \left[\frac{2R_{\text{wd}}}{\text{FWHM (cm/s)}} \right]^{2/3}, \quad (1)$$

where G is the gravitational constant. From the new HIRES dataset, we measure the FWHM of the C-S absorption feature assuming the line profile is Gaussian. With the resulting FWHM ~ 6 km/s, and the radius listed in Table 1, $R_{\text{Kep}} \sim 106 R_{\text{wd}}$ for WD 1124-293, a value almost double that in Debes et al. (2012) due to the high spectral resolution of the HIRES data. R_{Kep} is the best estimate of the minimum distance of the gas to the star and it depends on the width of the absorption feature. If the C-S absorption feature were more narrow, then R_{Kep} would be larger.

The outer edge of the gas is unknown, but we can consider a sublimation radius and a tidal disruption radius. The sublimation radius, R_{sub} is the distance at which the equilibrium temperature of particles equals their sublimation temperature, T_{sub} , with

$$R_{\text{sub}} = \frac{R_{\text{wd}}}{2} \left(\frac{T_{\text{wd}}}{T_{\text{sub}}} \right)^2. \quad (2)$$

This equation represents the smallest possible sublimation radius for optically thin distributions of dust and it assumes the particles absorb and emit radiation perfectly. R_{sub} depends on the shape, size, and composition of the particle. Graphite grains ($0.01 \mu\text{m}$) and astronomical silicate grains ($0.1 \mu\text{m}$) would sublimate at $54 R_{\text{wd}}$ and $93 R_{\text{wd}}$, respectively (see Figure 3). In Section 5, we discuss why the detectable gas at R_{Kep} is farther than R_{sub} .

The tidal disruption radius, R_{tide} (Davidsson 1999; Jura 2003; Veras et al. 2014), also depends on the composition of the material with

$$\frac{R_{\text{tide}}}{R_{\odot}} = C_{\text{tide}} \left(\frac{M_{\text{wd}}}{0.6 M_{\odot}} \right)^{1/3} \left(\frac{\rho_b}{3 \text{ g cm}^{-3}} \right)^{-1/3} \quad (3)$$

where C_{tide} has typical values of 0.85 to 1.89 (Bear & Soker 2013), and ρ_b , the density of the disrupting body satisfies $\rho_b \geq 1 \text{ g cm}^{-3}$ (Carry 2012; Veras et al. 2014). For WD 1124-293, the maximum tidal disruption radius is $R_{\text{tide}} \sim 200 R_{\text{wd}}$. We show typical ranges of tidal

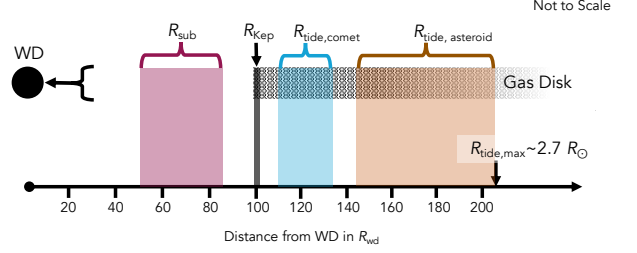


Figure 3. A not-to-scale cartoon of the model for WD gas and debris disks inspired by Metzger et al. (2012), where a solid debris disc typically forms near the tidal disruption radii which happens to be $\sim R_{\odot} \sim 120 R_{\text{wd}}$. There is no evidence that WD 1124-293 has a dusty debris disk, so we exclude it. The gas is shown with the speckled black and white region. We show 4 different radii R_{sub} , R_{Kep} , $R_{\text{tide,comet}}$, $R_{\text{tide,asteroid}}$ and a range of their possible values, with the shaded regions brought down to the axis for ease of reading, where applicable. The outer extent of the gas is unknown, as is the exact accretion mechanism. The maximum tidal radius for WD 1124-293 is $\sim 211 R_{\text{wd}} \sim 2.7 R_{\odot}$.

disruption radii for comets and asteroids ($R_{\text{tide,comet}}$ and $R_{\text{tide,asteroid}}$) in Figure 3.³

We take R_{Kep} as our minimum radius of the gas and assume that these radii follow the relation $R_{\text{tide}} > R_{\text{Kep}} > R_{\text{sub}}$ (see Figure 3). We set the gas to extend from $100 R_{\text{wd}}$ to $200 R_{\text{wd}}$ (approximately R_{Kep} to R_{tide}). The aspect ratio of the gas disk is $h/r \sim 10^{-3}$ (Metzger et al. 2012), so we truncate the gas to a cylinder with a height of 10% R_{wd} . We discuss the implications of this relation among radii in Section 5.

4.1.3. Hydrogen density

Most planetesimals accreted onto WDs are water poor, so there should be very little hydrogen gas present around WD 1124-293, assuming a planetesimal origin (see section 5.3 of Jura & Young 2014, and references therein). However, Cloudy uses the number density of hydrogen, n_{H} , to set the conditions of a cloud. If a C-S gas spectrum has features due to hydrogen, one could probe the maximum amount of hydrogen present in the system by calculating the column density due to H, N_{H} , assuming every H atom participates in the line transition. With no such features and a gas temperature too low for the Balmer $\text{H}\alpha$ line to form, we turn to a geometrical argument.

The area of the column along the line of sight which subtends the white dwarf is $\sim 2 \times H \times R_{\text{wd}}$ and the

³ For comparison, for comet Shoemaker Levy 9 had $C_{\text{tide}} \sim 1.31$ and $\rho_b \lesssim 0.702$ (Boss 1994), and would have a disruption radius of $\sim 110 R_{\text{wd}}$ near WD 1124-293.

volume is $2 \times H \times \Delta R \times R_{\text{wd}}^2$, where H is the gas height and $\Delta R = R_{\text{out}} - R_{\text{in}}$ is the gas extent in units of R_{wd} , with an outer radius, R_{out} , and an inner radius, R_{in} . The column density is equal to the number density times the volume of the gas column, divided by the area of the column along the line of sight which subtends the white dwarf. Solving for n_{H} ,

$$n_{\text{H}} \lesssim \frac{N_{\text{H}}}{\Delta R \cdot R_{\text{wd}}}. \quad (4)$$

We do not know the H number density, so we choose to explore a range such that $-1 \leq \log(n_{\text{H}}/\text{cm}^{-3}) \leq 10$. The minimum value is typical of the diffuse H II ($n_{\text{H}} \sim 0.3 - 10^4 \text{ cm}^{-3}$) and warm neutral medium ($n_{\text{H}} \sim 0.6 \text{ cm}^{-3}$) phases of the ISM (Draine 2011). For a maximum plausible value, we rely on observations of specific circumstellar disks around protoplanetary and transition disks.⁴ For gas with a height of $10\% R_{\text{wd}}$, extending from $100 R_{\text{wd}}$ to $200 R_{\text{wd}}$, with $\log N_{\text{H}} \sim 19$, $n_{\text{H}} \lesssim 10^9 \text{ cm}^{-3}$. We therefore explore the dependence of our models on the hydrogen density with a grid of models that have $-1 \leq \log(n_{\text{H}}/\text{cm}^{-3}) \leq 10$. For each model, the hydrogen density is constant with distance from the star. The most likely model is the one that minimizes the amount of H while allowing for metal lines to form.

4.1.4. C-S Gas Abundances

Calcium is the only C-S gas with a positive detection in WD 1124-293. Therefore, we consider the abundances of elements relative to Ca. Table 4 lists the elements that are typical pollutants of WDs for which we have photospheric abundance limits, and are thus explored with our modeling. We focus on the strongest optical transitions for these species that have photospheric detection (Mg I 3838 and Fe II 3228), and detection upper limits (K I 4043, Ni I 3480, Mn I 4032, Al I 3961, Si I 3905, Na I 5890). All other elements from He to Zn are left at the default solar composition values, relative to Ca. We approach the abundances in this way for two reasons. First, the ratios of potential metals of interest are very similar for a solar and chondritic composition (see Figure 6). Second, there is thus far only one detected C-S feature in the optical part of the spectrum for WD 1124-293. A UV spectrum would likely show more absorption features that could be used to better constrain the C-S metal abundances (see Figure 9).

We use the C-S column density of Ca II 3934 to constrain the modeling by varying the abundance ratios of

metals relative to calcium. Beginning with a hydrogen number density $n_{\text{H}} = 0.1 \text{ cm}^{-3}$ (a lower limit inspired by low density ISM regions), we first find abundance ratios that, when paired with the overall hydrogen density, result in optical depths that lead to a calculated absorption line with a depth at the 3σ limit to the observed continuum. For the rest of the metals considered, we ensured that their abundances were such that no lines were formed (see Figure 5). We then fix those abundance ratios and vary the hydrogen density over 10 orders of magnitude, while increasing the abundance of Ca relative to H to explore the model dependence on the amount of hydrogen present. The resulting grid of models is presented in Figure 4.

4.2. Cloudy Model Output

We choose to save the general overview, line optical depths, and line population for each Cloudy run. The general overview contains an output transmitted spectrum, but it does not include line broadening mechanisms, such as micro thermal motion, macro circular motion, or instrument effects, for an unresolved line. The net transmitted spectrum from Cloudy can however be used to check the validity of a set of input parameters (by investigating whether other absorption or emission features are produced), and to predict a spectrum ranging from the far UV to near IR (see Discussion).

We use the optical depth and column density to compare Cloudy models to MIKE spectrum. We save the optical depths, τ , for all species with $\tau > 0.001$ to calculate an absorption line profile, and the populations of upper and lower levels for all lines to calculate the column densities of different species. The column densities are calculated for each line by multiplying the lower level population per zone by the length of the zone. Zones are automatically calculated by Cloudy. We only consider the lower level populations in the column density calculation because we are not in a regime where stimulated emission is important.

5. RESULTS AND DISCUSSION

We investigate the gas toward WD 1124-293 to explore the conditions necessary to produce the observed absorption. We further constrain the location and amount of Ca present in the C-S gas, reproduce the observed C-S Ca K absorption line profile and place upper limits to the amounts of H, Mg, Ca, Fe, and other metals present around WD 1124-293 by using Cloudy to determine their optical depths and expected line column densities. We place limits on the total amount of gas and show the temperature profile through the model disk. We then connect these results to other similar studies and argue for future UV observations.

⁴ The maximum possible value of N_{H} for TW Hydrae is $\log(N_{\text{H}}/1 \text{ cm}^2) \sim 19.75$ (Herczeg et al. 2004), and the H column density for β Pictoris is $\log(N_{\text{H}}/1 \text{ cm}^2) \sim 18.6 \pm 0.1$, (Wilson et al. 2017).

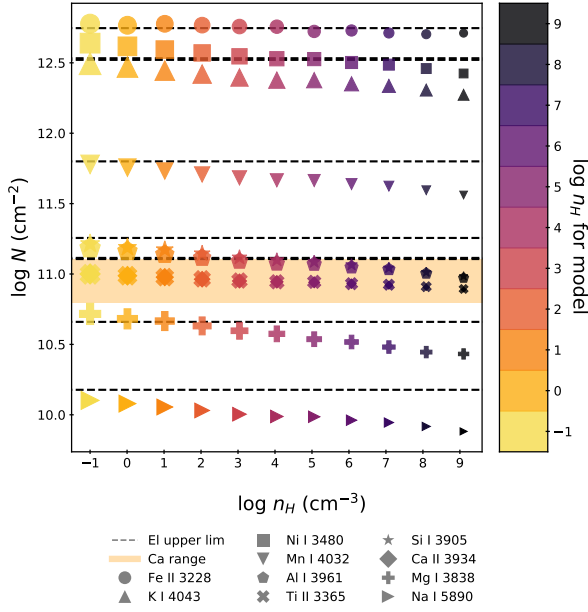


Figure 4. The column densities for a number of metal species in Cloudy models over hydrogen number densities from $\log n_H : -1$ to 9 [cm^{-3}]. The orange horizontal bar highlights the range of expected Ca II column densities (Debes et al. (2012) and this work), and the dashed lines highlight the maximum column densities for other species. The size of each marker is related to the absolute value of the element abundance. The metal abundances are not sensitive to the number density hydrogen.

5.1. Location of the gas

From the new HIRES observations, we show that the previously detected C-S and photospheric Ca gas is still present. Calcium in the atmosphere of WD 1124-293 has a settling time of ~ 1000 years (Dufour et al. 2017), so it is expected for the photospheric line to persist.

With the new observations we also find that the gas is farther away from WD 1124-293 than previously detected (Debes et al. 2012). Gaseous disks can accrete inward and spread outward due to angular momentum transport by turbulent viscosity (Metzger et al. 2012). However, why do we not observe gas at radii less than $100 R_{\text{wd}}$ if the gas is created through sublimation at smaller radii? Even with no IR excess due to dust grains, if the particle density is low enough, it is possible that destructive grain-grain collisions near the tidal disruption radius could be creating gas (Jura et al. 2007) at $R_{\text{Kep}} \sim 100 R_{\text{wd}}$. Alternatively, there could be a collection of sub-micron grains, which are inefficient emitters, and would thus sublimate at much larger distances than what would be assumed in a blackbody approximation. Emission features due to Ca in the spectra of SDSS J1228 + 1040 show that the gas in this system is

emitting at a range of radii ($0.6 - 1.2 R_{\odot}$ or $50 - 100 R_{\text{wd}}$), with a concentration at $\sim 100 R_{\text{wd}}$ (Manser et al. 2016).

5.2. Column Densities

We determine the column density of the C-S Ca gas by finding the range of optical depths that lead to an absorption feature at a depth of $\pm 3\sigma$ relative to the depth of the Ca C-S line in the MIKE dataset, resulting in $\log N(\text{Ca}) = 11.01^{+0.09}_{-0.26}$ (Debes et al. 2012 find $\log N(\text{Ca}) = 11^{+0.1}_{-0.2}$). The downward trend in column density with increasing hydrogen number density seen in Figure 4 is due to a decrease in the calculated electron density. To investigate the dependence of our modeling on hydrogen, we explored 10 orders of magnitude in hydrogen number density, fixing the relative abundance ratios for all elements. The hydrogen number density is degenerate with the hydrogen abundance, so we are only able to constrain the amount of hydrogen with a geometrical argument described in Section 4.2.2. The upper limits to the abundances of these different species are presented in Table 4.

5.3. Line Profiles

The Ca C-S absorption line is only marginally resolved, so we construct the absorption line profile by taking the convolution of (1) a Voigt line profile broadened due to Maxwellian distributed velocities and a gas temperature determined by Cloudy and (2) a Gaussian kernel with a width determined by the resolution of the HIRES spectrum.⁵ The Voigt line profile is approximated using a series expansion as $\phi(x) \propto \exp(-x^2) + a/(\pi^{1/2}x^2) + 2a/(\pi^{3/4}x^4)$, where a is the dampening constant for the transition in question, $x = (\nu - \nu_0)/\Delta\nu_{\text{Dopp}}$, ν_0 is the center frequency for line, and $\Delta\nu_{\text{Dopp}}$ is the FWHM of the line. The output intensity is $I = I_{\text{in}} \exp[-\tau\phi(x)]$, where τ is the optical depth at line center. The output intensity considering the velocity profile is $\propto \exp(-\tau[\phi(x) * \phi(v)])$.

We show the calculated line profiles for the strongest optical transitions of these metals in Figure 5.

5.4. Metals in the gas around WD 1124-293

The calculated calcium K line column density corresponds to an abundance of 1.35 relative to hydrogen when $n_{\text{H}} = 0.1 \text{ cm}^{-3}$. As we increased the hydrogen number density, we let the calcium and hydrogen abundances vary from $-8.90 < \log n(\text{Ca})/n(\text{H}) < 1.35$ and $-1 < \log n(\text{H}) < 11$. For the lowest H number density,

⁵ If the absorption line were resolved, we would also convolve the Voigt line profile with a velocity profile, $\phi(v)$ describing the bulk motion of the gas disk.

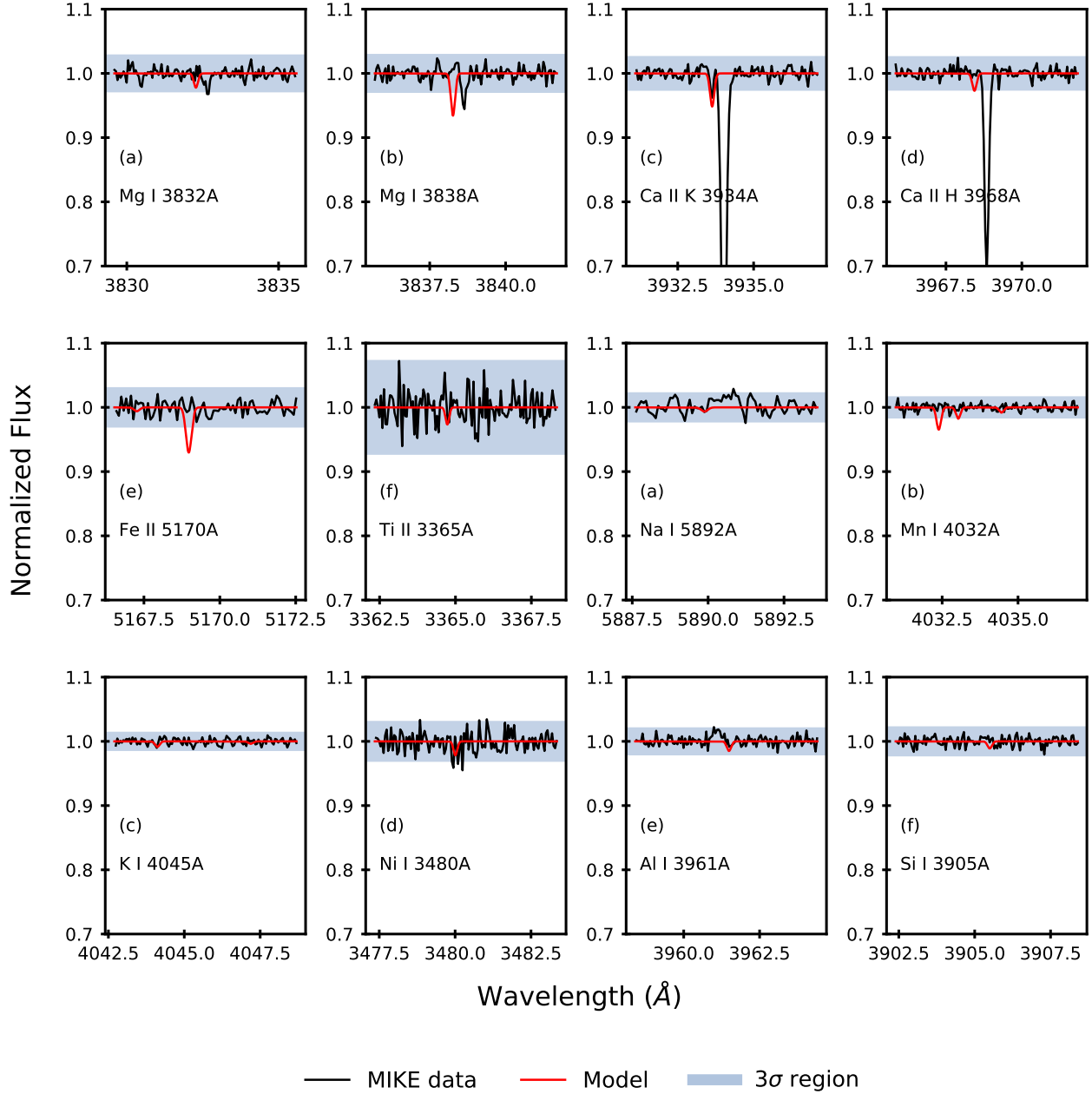


Figure 5. Calculated line profiles for species of interest. The calculated or model line profiles are shown in red. The black curves show the co-added MIKE spectra. The blue region highlights a $\pm 3\sigma$ region for the MIKE spectra. The strengths of the model absorption lines are limited by column density upper limits estimated from the MIKE spectrum. For the Ca features, the deeper photospheric component is gravitationally red-shifted.

the abundances of Mg and Fe that produce an absorption feature at a depth of 3σ are $\log n(\text{Mg})/n(\text{H}) = 7.85$ and $\log n(\text{Fe})/n(\text{H}) = 5.70$. We then fix the ratios of Mg and Fe relative to Ca with increasing density, such that $\log n(\text{Mg})/n(\text{Ca}) = 6.5$ and $\log n(\text{Fe})/n(\text{Ca}) = 4.4$ for all models shown in Figure 4. All other element abundances, El , are set such that $\log n(El)/n(\text{Ca})$ is constant for models with increasing n_{H} . Figure 4 shows how the

column density for the strongest observable optical transition in a species varies with increasing H number density and fixed element abundance ratios.

5.5. The mass of the gas around WD1124-293

Given our geometrical constraints (inner radius, R_{in} and outer radius, R_{out}) and assumed disk height, H , the volume of the gas disk is $V = \pi H(R_{\text{out}}^2 - R_{\text{in}}^2)$, and the

Table 4. Photospheric and Circumstellar Metal Abundances and Masses

El	Phot	$\log \dot{M}(El)$	C-S	$\log M_{C-S}$
		(g yr^{-1})		(g)
H	1	—	1	< 5.95
Na	< -8.30	< 13.62	< 3.35	< 10.67
Mg	-7.689 ± 0.024	14.30	< 7.85	< 15.19
Al	< -8.80	< 13.24	< 7.05	< 14.44
Si	< -7.50	< 14.54	< 6.65	< 14.06
K	< -8.00	< 14.20	< 7.05	< 14.61
Ca	-8.872 ± 0.188	13.33	$1.357^{+0.086}_{-0.257}$	$8.92^{+0.1}_{-0.3}$
Ti	< -8.50	< 13.86	< 1.2	< 8.84
Mn	< -8.50	< 14.01	< 4.65	< 12.34
Fe	-7.814 ± 0.130	14.69	< 5.7	< 13.40
Ni	-8.40	< 14.10	< 5.35	< 13.08
Total				< 15.38

NOTE— Photospheric and circumstellar (C-S) abundances by number relative to hydrogen, $\log n(El)/n(H)$, for our model. We show the C-S abundances that corresponding to a model with $n_H = 0.1 \text{ cm}^{-3}$.

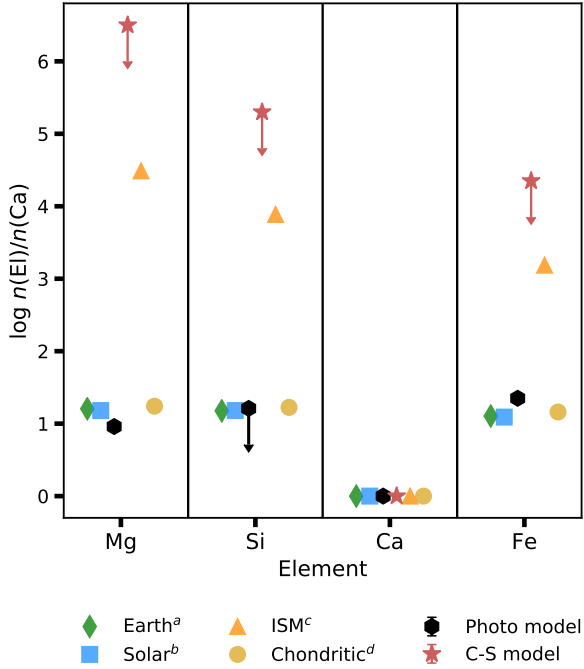


Figure 6. Abundances relative to calcium for metals typically present in photospheric pollution of WDs. We show the upper limits for our Cloudy model with $n_H = 0.1 \text{ cm}^{-3}$ with the star markers and the abundances derived from the photospheric model considering diffusion with the black hexagons. We only had a marginal detection of silicon in the photosphere and provide an upper limit there. ^aAllègre et al. (2001), ^bHolweger (2001); Grevesse & Sauval (1998), ^cCowie & Songaila (1986), and ^dLodders (2003).

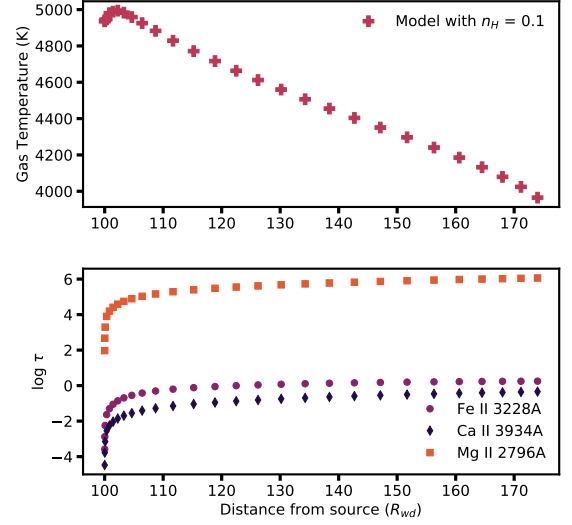


Figure 7. Top panel: The temperature profile through the disk. Some useful output from Cloudy is the ability to know the temperature profile within the cloud. Modeling of regions usually assume an isothermal environment which is not the case for many of the models. Lower panel: Optical depth with distance for the Ca K line, as well as the Fe and Mg lines responsible for heating and cooling, respectively.

total gas mass M_{tot} is given by

$$M_{\text{tot}} = V \cdot \left[\sum (10^{n_H} \cdot 10^{\text{abn}} \cdot m_{\text{El}}) + 10^{n_H} \right] \cdot m_H, \quad (5)$$

where n_H is the hydrogen number density, abn is the abundance relative to hydrogen, m_{El} is the mass of an element in atomic mass units, and m_H is the mass of the hydrogen atom in g. Using the abundances and hydrogen density from our model with a maximum amount of hydrogen ($n_H = 10^9 \text{ cm}^{-3}$), we place an upper limit on the total gas mass, $\log M_{\text{tot}} \approx 16.12 \text{ g}$ or ~ 30 times the mass of C-type asteroid 162173 Ryugu ($4.50 \times 10^{14} \text{ g}$, Watanabe et al. 2019). Using our model with a minimum amount of hydrogen ($n_H = 10^{-1} \text{ cm}^{-3}$), the upper limit on the total gas mass is $\log M_{\text{tot}} = 15.38 \text{ g}$ or ~ 5 times the mass of Ryugu. The lower limit is set by the total amount of mass required to produce the Ca feature, so the C-S gas mass, $\log M_{C-S}$ is constrained to $8.92 < \log M_{C-S} < 16.12$. Figure 6 shows the relative abundances of Mg, Si, Ca, and Fe for our best fit and the relative abundances of those same metals in the photosphere.

5.6. Gas Temperature

Cloudy also provides the temperature throughout the gas. For this model, the gas temperature ranges from $\sim 4994 \text{ K}$ to $\sim 3965 \text{ K}$. We show the temperature profile for the best fit model in Figure 7, also including the

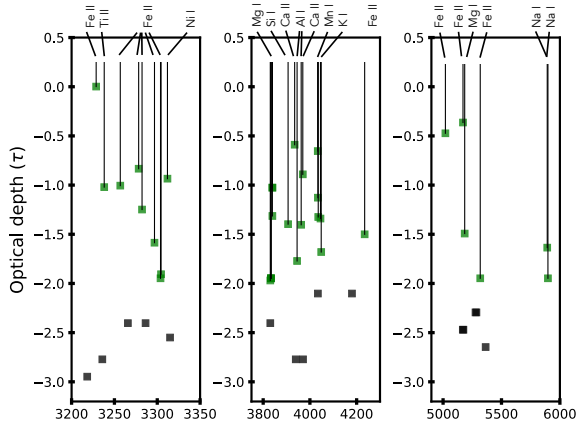


Figure 8. Optical depths versus wavelengths of the strongest species for our model with the maximum amount of hydrogen. The green squares highlight lines with optical depths > -2.0 and the black squares arise from different Mg, Ca, and Fe species. There are many Mg I lines at $\sim 3800\text{\AA}$, though we only show one label for reading legibility.

optical depths of the two strongest lines at the same depths in the disk.

In our Cloudy models, the heating is dominated by Fe II and the cooling is dominated by Mg II (see bottom panel of Figure 7). The temperature of the gas is determined by Cloudy self-consistently and depends on heating and cooling mechanisms. Other efforts to model C-S around WDs tend to assume the temperature is isothermal, though at least one group calculates the temperature at different locations in the disk assuming a Shakura and Sunyaev viscous α -disk using the accretion-disk code AcDc (Hartmann et al. 2016; Nagel et al. 2004). For a WD with $T_{\text{eff}} = 20900\text{ K}$, Hartmann et al. (2016) find the gas temperature decreases to a minimum value $\sim 6000\text{ K}$ a third of the way through the disk before rising to a maximum of $\sim 6600\text{ K}$ at the outer edge. The temperature profile of this gas disk is very different from that of WD 1124-293, as shown in the top panel of Figure 7. For WD 1124-293, the gas temperature profile declines roughly as the $T \propto r^{-0.35}$, with a mild inversion at the inner edge of the disk. Further investigation is needed to understand this discrepancy. Additionally, for hotter WDs, the temperature range probed by Cloudy could be much larger than the 20% changes seen for WD 1124-293.

5.7. Strongest transitions and a need for UV observations

The strongest expected lines in the optical come from the enhanced Mg, Ca, and Fe in our solar-like composition around WD1123-293 (see Figure 8). To obtain the

abundances of heavy elements for the photosphere, we proceed in a similar way as described in Xu et al. (2019), by computing grids of synthetic spectra for each element of interest using a pure DA atmospheric structure assuming the stellar parameters previously determined by fitting the photometric data and parallax measurement. The abundances are then obtained by minimizing χ^2 between the normalized spectroscopic data and the grid spectrum. Trace amounts of metals have a negligible effect on the thermodynamic structure for the grid spectrum.

The strongest transitions for most of these species that would help constrain the gas composition and therefore, the sublimation temperature (O, Fe, Si, and Mg), are in the UV. Our polluted photospheric model for WD 1124-293 predicts very strong Mg and Fe absorption lines at UV wavelengths, and as such, our upper limits are likely too large (see Figure 9).

FUV observations of other dusty WDs with $T_{\text{eff}} \geq 12000\text{ K}$ have shown absorption lines from as many as 19 unique elements (GD 362, Xu et al. 2013), providing detailed information about planetary material that orbits another star. For example, we can look for correlations between progenitor mass and elemental abundance, or seek to find correlations with specific elemental enhancements, such as Ca. With UV observations, better constraints would be placed on Mg and Fe, helping to further constrain the relative abundances of these metals.

5.8. Other work modeling WDs with Cloudy

Gänsicke et al. (2019) use Cloudy to model the C-S gas of WD J0914+1914 viewed in emission, which contains signatures of the disruption and subsequent accretion of a giant planet. WD J0914+1914 has $T_{\text{eff}} = 27743 \pm 310\text{ K}$ and its photosphere shows evidence of ongoing accretion of oxygen and sulfur. At this temperature, the C-S gas is photoionized, and contains enough hydrogen for oxygen, sulfur, and H α emission lines to form. The emission features are doubly peaked, indicating the gas is in disk undergoing Keplerian rotation. In their work, the C-S abundances for O and S are consistently determined by two independent methods for the first time.

With this work, we follow up with the second instance to date of determining gas composition with two independent measurements, and show for the first time how to place constraints on abundances when only absorption features are present. This proof of concept for modeling absorption with Cloudy will be useful when applied to more complicated systems, such as WD 1145+017.

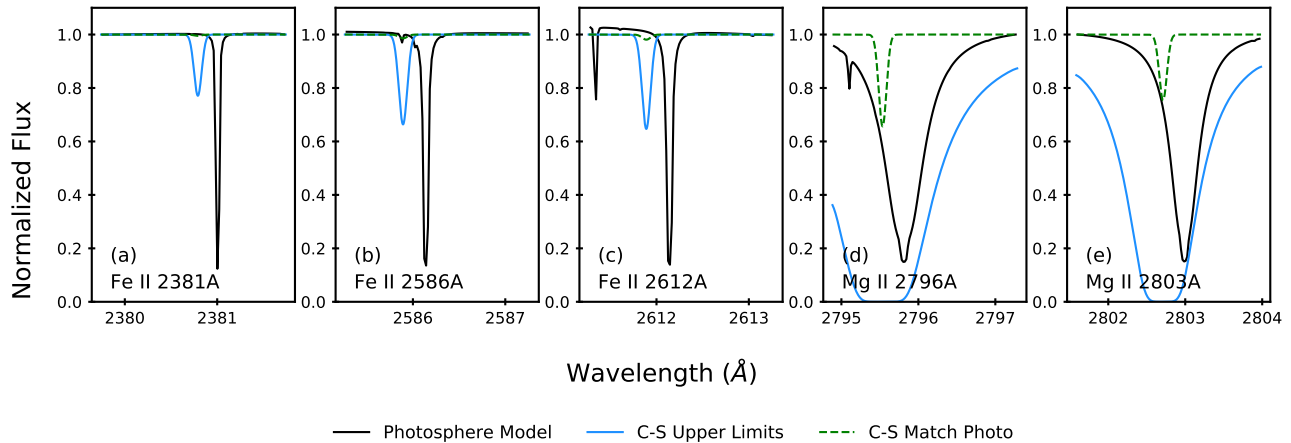


Figure 9. Predicted UV line profiles for Mg and Fe. The models presented in our results section extend into the UV, so we explore two cases. In the first case, we set the abundance ratios of Mg/Ca and Fe/Ca to match the photospheric values. The solid black line is the best fit polluted photospheric model for WD 1124-293. In the second case, we set the abundance ratios at the modeled upper limits. The expected profiles for Fe/Ca and Mg/Ca equal to the photospheric abundance ratios are shown with the dashed green line. The expected profiles for the C-S abundance upper limits are shown with a solid blue line.

5.9. Our proof of concept in the context of WD 1145+017

WD 1145+017 was first shown to have a transiting, disintegrating planetesimal by [Vanderburg et al. \(2015\)](#) and has been since been the subject of much observation (e.g. [Xu et al. 2016](#); [Cauley et al. 2018](#); [Croll et al. 2017](#); [Xu et al. 2019](#); [Fortin-Archambault et al. 2020](#)) due to days to week transit and spectroscopic variability. [Fortin-Archambault et al. \(2020\)](#) present a new characterization of WD 1145+017’s absorption features, showing how a simple model of nested concentric rings with high eccentricity can help account for the majority of the observed features, which include asymmetrical line profiles and Doppler shifting of the absorption features. These features are also seen in a number of other polluted WDs showing emission lines (e.g., [Wilson et al. 2014](#); [Manser et al. 2019](#); [Gänsicke et al. 2019](#)).

The addition of high-resolution spectra to the analysis in [Fortin-Archambault et al. \(2020\)](#) helped disentangle closely spaced features that led to an overestimated prior abundance calculation in [Xu et al. \(2016\)](#). A code like Cloudy could be useful in identifying components of such blends to obtain accurate abundances. They also observe Si IV features in the UV at 1393.76Å and 1402.77Å and invoke an additional low eccentricity component to explain the presence of such highly ionized species. Cloudy would naturally be able to probe the conditions needed to produce Si IV features with its self-consistent microphysics.

6. CONCLUSION

With this work, we outline how to use the Cloudy radiative transfer code to model C-S gas viewed in ab-

sorption around WD 1124-293. We create a Cloudy grid of models for C-S gas around WD 1124-293 to explore the abundances of elements from He to Zn relative to hydrogen, and obtain line optical depths, species column densities, and the temperature profile through the gas disk. Our best fit model minimizes the total amount of hydrogen, while still producing the observed Ca K C-S absorption feature.

We detect photospheric absorption features due to Mg and Fe for the first time, determine a new location for the C-S gas, and place upper limits on abundances of other metals in the photosphere. The upper limit C-S abundance ratios of Mg, Si, and Fe to Ca are also consistent with the photospheric abundance ratios, and with a chondritic/bulk Earth composition.

With these models, we place constraints on the potential masses and abundances that could result in a spectrum dominated by calcium species for WD 1124-293, find that the C-S is likely not isothermal, and show that the Cloudy microphysics code, which is typically used to model active galactic nuclei and HII regions, can also be used to model C-S gas absorption features of polluted white dwarfs. UV spectroscopic observations of WD 1124-293 are needed to further constrain the composition of its C-S gas.

Looking forward, we intend to explore the properties of C-S gas around DA WDs with temperatures 6000 K to 27,000 K using Cloudy, and will make the grid of gas properties publicly available (Steele et al. *in prep*).

We thank the Referee for their helpful comments. We thank the W. M. Keck Observatory Visiting Scholars Program for hosting A. Steele for 7 weeks. Special

thanks go to Dr. Sherry Yeh and Dr. Carlos Alvarez for their guidance during the program. Additional thanks go to Dr. Jordan Steckloff for helpful conversations about sublimation near white dwarfs; and to Dr. Drake Deming and Dr. Siyi Xu for providing financial support for this work.

This work has made use of data from the European Space Agency (ESA) mission *Gaia* (<https://www.cosmos.esa.int/gaia>), processed by the *Gaia* Data Processing and Analysis Consortium (DPAC, <https://www.cosmos.esa.int/web/gaia/dpac/consortium>). Funding for the DPAC has been provided by national institutions, in particular the institutions participating in the *Gaia* Multilateral Agreement. This work is supported by the international Gemini Observatory, a program of NSF's NOIRLab, which is managed by the Association of Universities for Research in Astronomy (AURA)

under a cooperative agreement with the National Science Foundation, on behalf of the Gemini partnership of Argentina, Brazil, Canada, Chile, the Republic of Korea, and the United States of America. Some of the data presented herein were obtained at the W. M. Keck Observatory, which is operated as a scientific partnership among the California Institute of Technology, the University of California and the National Aeronautics and Space Administration. The Observatory was made possible by the generous financial support of the W. M. Keck Foundation.

Facilities: Magellan(MIKE), Keck(HIRES)

Software: astropy (Astropy Collaboration et al. 2013), Cloudy (Ferland et al. 2017), PyAstronomy (Czesla et al. 2019)

REFERENCES

- Allègre, C., Manhès, G., & Lewin, É. 2001, *Earth and Planetary Science Letters*, 185, 49
- Astropy Collaboration, Robitaille, T. P., Tollerud, E. J., et al. 2013, *A&A*, 558, A33
- Barber, S. D., Belardi, C., Kilic, M., et al. 2016, *MNRAS*, 459, 1415
- Bear, E., & Soker, N. 2013, *NewA*, 19, 56
- Bernstein, R., Shtetman, S. A., Gunnels, S. M., et al. 2003, *Proc. SPIE*, 1694
- Boss, A. P. 1994, *Icarus*, 107, 422
- Carry, B. 2012, *Planet. Space Sci.*, 73, 98
- Cauley, P. W., Farihi, J., Redfield, S., et al. 2018, *ApJL*, 852, L22
- Cowie, L. L., & Songaila, A. 1986, *ARA&A*, 24, 499
- Croll, B., Dalba, P. A., Vanderburg, A., et al. 2017, *ApJ*, 836, 82
- Czesla, S., Schröter, S., Schneider, C. P., et al. 2019, *PyA: Python astronomy-related packages*, ascl:1906.010
- Davidsson, B. J. R. 1999, *Icarus*, 142, 525
- Debes, J. H., Kilic, M., Faedi, F., et al. 2012, *ApJ*, 754, 59
- Draine, B. T. 2011, *Physics of the Interstellar and Intergalactic Medium* by Bruce T. Draine. Princeton University Press
- Dufour, P., Blouin, S., Coutu, S., et al. 2017, 20th European White Dwarf Workshop, 3
- Dupuis, J., Fontaine, G., Pelletier, C., et al. 1993, *ApJS*, 84, 73
- Dupuis, J., Fontaine, G., & Wesemael, F. 1993, *ApJS*, 87, 345
- Ferland, G. J., Chatzikos, M., Guzmán, F., et al. 2017, *RMxAA*, 53, 385
- Fortin-Archambault, M., Dufour, P., & Xu, S. 2020, *ApJ*, 888, 47
- Gaia Collaboration, Brown, A. G. A., Vallenari, A., et al. 2018, *A&A*, 616, A1
- Gänsicke, B. T., Schreiber, M. R., Toloza, O., et al. 2019, *Nature*, 576, 61
- Grevesse, N., & Sauval, A. J. 1998, *SSRv*, 85, 161
- Hartmann, S., Nagel, T., Rauch, T., et al. 2016, *A&A*, 593, A67
- Herczeg, G. J., Wood, B. E., Linsky, J. L., et al. 2004, *ApJ*, 607, 369
- Holweger, H. 2001, Joint SOHO/ACE Workshop “solar and Galactic Composition”, 23
- Jura, M. 2003, *ApJL*, 584, L91
- Jura, M., Farihi, J., & Zuckerman, B. 2007, *ApJ*, 663, 1285
- Jura, M., & Young, E. D. 2014, *Annual Review of Earth and Planetary Sciences*, 42, 45
- Kobayashi, H., Kimura, H., Watanabe, S.-i., et al. 2011, *Earth, Planets, and Space*, 63, 1067
- Koester, D., Gänsicke, B. T., & Farihi, J. 2014, *A&A*, 566, A34
- Koester, D. 2009, *A&A*, 498, 517
- Koester, D. 2010, *Mem. Soc. Astron. Italiana*, 81, 921
- Lodders, K. 2003, *ApJ*, 591, 1220
- Manser, C. J., Gänsicke, B. T., Marsh, T. R., et al. 2016, *MNRAS*, 455, 4467
- Manser, C. J., Gänsicke, B. T., Eggl, S., et al. 2019, *Science*, 364, 66
- Metzger, B. D., Rafikov, R. R., & Bochkarev, K. V. 2012, *MNRAS*, 423, 505

- Nagel, T., Dreizler, S., Rauch, T., et al. 2004, *A&A*, 428, 109
- Subasavage, J. P., Jao, W.-C., Henry, T. J., et al. 2017, *AJ*, 154, 32
- Tremblay, P.-E., & Bergeron, P. 2009, *ApJ*, 696, 1755
- Vanderburg, A., Johnson, J. A., Rappaport, S., et al. 2015, *Nature*, 526, 546
- Veras, D., Leinhardt, Z. M., Bonsor, A., et al. 2014, *MNRAS*, 445, 2244
- Vogt, S. S., Allen, S. L., Bigelow, B. C., et al. 1994, *Proc. SPIE*, 362
- Watanabe, S., Hirabayashi, M., Hirata, N., et al. 2019, *Lunar and Planetary Science Conference*, 1265
- Wilson, D. J., Gänsicke, B. T., Koester, D., et al. 2014, *MNRAS*, 445, 1878
- Wilson, P. A., Lecavelier des Etangs, A., Vidal-Madjar, A., et al. 2017, *A&A*, 599, A75
- Xu, S., Hallakoun, N., Gary, B., et al. 2019, *AJ*, 157, 255
- Xu, S., Dufour, P., Klein, B., et al. 2019, *AJ*, 158, 242
- Xu, S., Jura, M., Klein, B., et al. 2013, *ApJ*, 766, 132
- Xu, S., Jura, M., Dufour, P., et al. 2016, *ApJL*, 816, L22